Adaptive Superpixel Segmentation of Marine SAR Images by Aggregating Fisher Vectors

Xueqian Wang, *Member, IEEE*, You He, Gang Li, *Senior Member, IEEE*, and Antonio Plaza, *Fellow, IEEE*

***Abstract*—Superpixel segmentation is an important technique for image analysis. In this article, we develop a new superpixel segmentation approach and investigate its application on ship target detection in marine synthetic aperture radar (SAR) images. Existing superpixel segmentation algorithms often simply consider the intensity and spatial features, which may degrade the segmentation performance due to the low contrast between ship targets and the sea clutter background in marine SAR images. Besides, it is difficult for existing algorithms to adaptively select the weights of the features. Here, we propose a new Fisher vector (FV)-based adaptive superpixel segmentation (FVASS) algorithm to address the aforementioned issues. Our newly developed FVASS not only fuses the intensity and spatial features, but also the multiorder features introduced by FVs, resulting in a better segmentation performance (even with low signal-to-clutter ratios). The weights of the features considered in FVASS are adaptively adjusted by minimizing the sum of within-superpixel variances to maintain the compactness of superpixels. Experiments demonstrate that, compared with commonly used superpixel segmentation methods, the proposed FVASS algorithm enhances the segmentation performance of SAR images and further improves the detection performance of existing superpixel-based ship detectors.**

***Index Terms*—Fisher vectors (FVs), ship detection, superpixel segmentation, synthetic aperture radar (SAR).**

I. Introduction

SYNTHETIC aperture radar (SAR) is a widely applied technology for ocean monitoring/management, including ship target detection, due to its ability to generate high-resolution images under all-weather and day-or-night conditions [1], [2]. In the last decades, more and more marine SAR images have been collected with the extensive development of SAR systems. Therefore, it is necessary to develop effective and automatic methods for marine SAR image processing.

Superpixels represent locally coherent and visually significative image regions, which can reveal the boundary and structure information of the targets in marine SAR images [2]–[19]. Besides, the degeneration of target detection/discrimination performance caused by speckle noise in SAR images can be alleviated by using superpixel-level features [8]. Superpixels can also reduce the subsequent image processing time, such as superpixel-based ship detection in marine SAR images [7].

Regarding the problem of generating superpixels, there are the following two key tasks: 1) how to select pixel features, and 2) how to assign weights to such features in the calculation of pixel distances to achieve the local clustering. Recently, some works have been devoted to these two tasks in the context of superpixel segmentation of SAR images [6]–[19].

A very popular approach for superpixel segmentation is simple linear iterative clustering (SLIC) [9]. This algorithm was first proposed for optical image segmentation, where the CIELAB color feature and the spatial features of pixels are used to locally cluster pixels into superpixels. In [10], the CIELAB color feature in SLIC is replaced by the intensity feature to make SLIC more suitable for the segmentation of SAR images. Instead of the intensity feature of isolated pixels, the patch-based intensity feature is considered in [7] and [8] to reduce the effect of image noise on superpixel segmentation. In [11] and [12], the commonly used spatial feature calculated with Euclidean distance is extended to the Mahalanobis distance and Wishart distance, respectively, to improve the segmentation performance. Note that the abovementioned superpixel segmentation algorithms in [7]–[12] mainly focus on simple intensity and spatial features of pixels and may provide an unsatisfactory segmentation performance for marine SAR images, due to the strong sea clutter background and relatively weak ship targets therein [20]. In addition, it is difficult to determine the weights of the intensity and spatial features considered in [7]–[12] to balance them properly in marine SAR images with different signal-to-clutter ratios (SCRs).

In [13]–[18], the edge information and the local directional change of intensity are considered as new features to improve the segmentation performance for SAR images in urban/land environments. In [13] and [18], edges in polarimetric SAR images are utilized to achieve superpixel segmentation based on the spherically invariant random vector model. In [14], the image

Manuscript received July 2, 2020; revised December 3, 2020; accepted January 10, 2021. Date of publication January 13, 2021; date of current version February 3, 2021. This work was supported in part by the National Natural Science Foundation of China under Grant 61790551 and Grant 61925106, in part by the Civil Space Advance Research Program of China under Grant D010305, in part by the Postdoctoral Innovative Talent Support Program under Grant BX20200195, in part by the China Postdoctoral Science Foundation under Grant 2020M680561, in part by the Shuimu Tsinghua Scholar Program, and in part by the FEDER and Junta de Extremadura under Grant GR18060. This work has been presented in part at the IEEE International Geoscience and Remote Sensing Symposium, Waikoloa, Hawaii, Septemper 2020 [19]. *(Corresponding author: You He.)*

Xueqian Wang and Gang Li are with the Department of Electronic Engineering, Tsinghua University, Beijing 100084, China (e-mail: wangxueqian@mail.tsinghua.edu.cn; gangli@tsinghua.edu.cn).

You He is with the Institute of Information Fusion, Naval Aeronautical University, Yantai 264001, China, and also with the Department of Electronic Engineering, Tsinghua University, Beijing 100084, China (e-mail: heyou@mail.tsinghua.edu.cn).

Antonio Plaza is with the Hyperspectral Computing Laboratory, Department of Technology of Computers and Communications, Escuela Politécnica, University of Extremadura, 10003 Cáceres, Spain (e-mail: aplaza@unex.es).

Digital Object Identifier 10.1109/JSTARS.2021.3051301

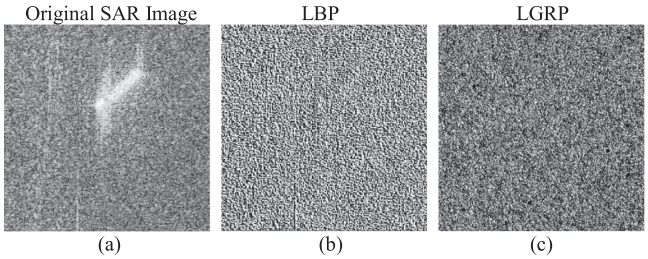

Fig. 1. Examples of two gradient features of marine SAR images. (a) Original SAR image. (b) LBP [21] of (a). (c) LGRP [14] of (a). Here, a 3 × 3-pixel window is used to calculate LBP and LGRP.

gradient of SAR images is calculated to measure the variation coefficient within superpixels. In [16] and [17], Gaussian and Gabor templates are used to calculate the edge maps of SAR images to enhance the compactness of superpixels. In particular, the weights of the features are adaptively adjusted in [13] and [14], according to the local homogeneity degree of SAR images. However, the exact edges and gradients of SAR images in *marine* environments are often severely contaminated by the widely strong and heterogeneous sea clutter background [4]. In Fig. 1, we show two kinds of gradient features in marine SAR images, i.e., local binary pattern (LBP) [21] and local gradient ratio pattern (LGRP) [14]. In both cases, it is difficult to distinguish the target from the clutter background, indicated that more robust strategies are required for superpixel segmentation in marine SAR images.

The Fisher vector (FV) is another widely used feature. It models the difference between the pixel under test and the global Gaussian mixture model (GMM) of the image [23], [24]. This difference is measured by the gradient of the log-likelihood with respect to the weights, mean values, and standard deviations in the GMM, which are termed as the zero-order, first-order, and second-order information contained in the FV of the pixel [23]. Compared with the intensity feature [7]–[12], the FV is a more informative feature that provides multiorder information about the pixels. To the best of authors' knowledge, the FV feature has never been exploited to improve the superpixel segmentation of marine SAR images.

Main Contribution: In this article, we propose a new FV-based adaptive superpixel segmentation (FVASS) algorithm for marine SAR images and further investigate its application to ship target detection problems. In addition to commonly used intensity and spatiality features, three new features, i.e., the zero-order, first-order, and second-order information contained in FVs are exploited by the proposed FVASS algorithm to improve the superpixel segmentation performance of marine SAR images, especially with low SCRs. Besides, the weights of the features are adaptively adjusted in the iterations of FVASS to enhance the compactness of superpixels. Note that the strategy adopted for balancing such weights is different from the one adopted in [13], [14]. Specifically, the feature weights in the proposed FVASS method are selected according to the relative importance of all the features (instead of the value of a specific feature, e.g., homogeneity degree of the SAR images, as in [13] and [14]). Our experimental results demonstrate that: 1) the proposed FVASS algorithm provides a better segmentation performance than other existing, commonly used approaches; 2) FVASS further improves the performance of ship detection when it is adopted for the superpixel segmentation step in existing superpixel-based detection frameworks.

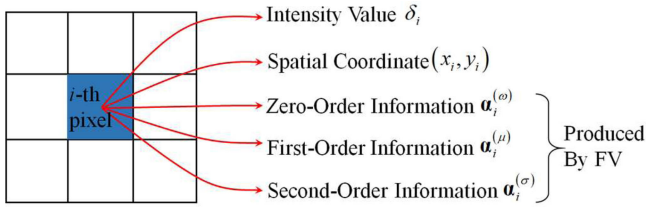

Fig. 2. Pixel feature representation for superpixel generating.

The remaining content of this article is organized as follows. Section II formulates the intensity feature, spatiality feature, and the multiorder features in FVs considered for superpixel segmentation. In Section III, we develop a new feature discriminability measure to calculate the distance of two pixels in SAR images. In Section IV, we design the adaptive weights of the features and elaborate on the proposed FVASS algorithm. Section V provides in-depth comparisons between the proposed FVASS algorithm and other existing algorithms via detailed experiments. Section VI concludes this article with some remarks and hints at plausible future research.

II. Feature Representation

The selection of features plays an important role in superpixel segmentation. Intensity and spatiality features are two commonly used pixel features for such purpose. Existing superpixel segmentation algorithms [7]–[12] completely depending on these two features may achieve the nonideal segmentation in low SCR scenarios. In [10] and [20], the zero-order, first-order, and second-order features produced by FVs were shown to be effective and robust in terms of distinguishing ship targets from sea clutter, but these features have not been exploited as of yet for the problem of superpixel segmentation in SAR images. In this section, we introduce an improved pixel feature representation for superpixel segmentation, which not only incorporates the intensity and spatiality features, but also the multiorder features contained in FVs, as shown in Fig. 2.

A. Intensity Feature

In general, ship targets appear as bright parts with larger intensity values than the clutter background in SAR images, as shown in Fig. 1(a). Following this idea, the intensity feature is a straightforward one for superpixel segmentation. Let δ_i denote the intensity value of the ith pixel in the SAR image, where $i = 1,2,\ldots, I$, and I is the total number of pixels in the SAR image.

B. Spatiality Feature

The spatial coordinates of pixels are helpful to generate locally meaningful regions [22]. The spatiality feature of the ith pixel is represented by (x_i, y_i), where x_i and y_i are the horizontal and vertical locations of the ith pixel, for $i = 1,2,\ldots, I$.

C. Multiorder Features in FVs

GMM provides the capability to model any continuous distribution in terms of a linear combination of different Gaussian distributions [25]. A GMM can be completely specified by its parameter set $\mathbf{\Lambda} \triangleq \{\omega_m, \mu_m, \sigma_m, m = 1, 2, \ldots, M\}$, where ω_m, μ_m, and σ_m are the weight, mean value, and standard deviation of the *m*th Gaussian distribution in the mixture, respectively, and *M* is the number of Gaussian distributions. The parameter set $\mathbf{\Lambda} = \{\omega_m, \mu_m, \sigma_m, \forall m\}$ of GMM can be pre-estimated by using maximum likelihood estimation methods [26].

The FV $\mathbf{a}_i \in \mathbb{R}^{3M\times 1}$ of the *i*th pixel in the SAR image is calculated as the normalized gradient vector with respect to the GMM parameters in $\mathbf{\Lambda}$ [23]

$$\mathbf{a}_i = [\underbrace{a_{i,\omega_1}, \ldots, a_{i,\omega_M}}_{\left(\mathbf{a}_i^{(\omega)}\right)^T}, \underbrace{a_{i,\mu_1}, \ldots, a_{i,\mu_M}}_{\left(\mathbf{a}_i^{(\mu)}\right)^T}, \underbrace{a_{i,\sigma_1}, \ldots, a_{i,\sigma_M}}_{\left(\mathbf{a}_i^{(\sigma)}\right)^T}]^T \tag{1}$$

where $a_{i,\omega_m} = (\phi_{i,m} - \beta_m)/\sqrt{\beta_m}$, $a_{i,\mu_m} = \phi_{i,m}(\frac{\delta_i - \mu_m}{\sigma_m\sqrt{\beta_m}})$, $a_{i,\sigma_m} = \frac{\phi_{i,m}}{\sqrt{2\beta_m}}[\frac{(\delta_i-\mu_m)^2}{\sigma_m^2} - 1]$, $\beta_m = \frac{\exp(\omega_m)}{\sum_{\bar{m}=1}^{M}\exp(\omega_{\bar{m}})}$, $\phi_{i,m} = \frac{\omega_m f_m(\delta_i)}{\sum_{\bar{m}=1}^{M}\omega_{\bar{m}} f_{\bar{m}}(\delta_i)}$, $f_m(\cdot)$ are the *m*th Gaussian distribution in GMM, i = 1,2,…,*I*, and m = 1,2,…,*M*. From (1), we have that $\mathbf{a}_i^{(\omega)}$, $\mathbf{a}_i^{(\mu)}$, and $\mathbf{a}_i^{(\sigma)}$ represent the zero-order, first-order, and second-order features in the FV $\mathbf{a}_i$, respectively. Then, intrasign-square-rooting is performed on $\mathbf{a}_i^{(\omega)}$, $\mathbf{a}_i^{(\mu)}$, and $\mathbf{a}_i^{(\sigma)}$, respectively, to avoid the FV to be close to null [23]. After (1), $\mathbf{a}_i^{(\omega)}$, $\mathbf{a}_i^{(\mu)}$, and $\mathbf{a}_i^{(\sigma)}$ are self-l_2-normalized, respectively, for fair comparison in Section III [see (5)].

In [10] and [20], FVs were used to encode superpixels in the SAR image. The FV defined in (1) is an extended version of that in [10] and [20]. In detail, the FV in this article is pixel-wise, while the FV is made superpixel-wise in [10] and [20] by mean-pooling all the pixel-wise FVs in a superpixel. Pixel-wise FVs enrich the representation of pixels and have not been exploited for superpixel segmentation thus far.

Based on Section II-A.C, the proposed pixel feature representation is

$$\mathbf{\Omega}(i) \triangleq \left\{\delta_i, (x_i, y_i), \mathbf{a}_i^{(\omega)}, \mathbf{a}_i^{(\mu)}, \mathbf{a}_i^{(\sigma)}\right\} \quad \forall i \tag{2}$$

which aggregates the intensity and spatiality features, and also the zero-order, first-order, and second-order features produced by FVs.

III. Distance Measure

In addition to feature selection, another key problem for superpixel segmentation is how to calculate the distance between two pixels in feature space. In this section, we introduce a distance measure based on the aggregative pixel feature representation in (2), where the importance of each feature is represented by its weight.

First, we define the distances of intensity features, spatiality features, and the zero-order, first-order, and second-order features of FVs between pixel *i* and pixel *j* as follows:

$$d_1(i,j) = \sum_{t=1}^{T} G(t) \times |\delta_{i_t} - \delta_{j_t}| \tag{3}$$

$$d_2(i,j) = \sqrt{(x_i - x_j)^2 + (y_i - y_j)^2} \tag{4}$$

$$d_{3,4,5}(i,j) = \sum_{t=1}^{T} G(t) \times \left\|\mathbf{a}_{i_t}^{(\omega,\mu,\sigma)} - \mathbf{a}_{j_t}^{(\omega,\mu,\sigma)}\right\|_2 \tag{5}$$

where $i, j \in \{1, 2, \ldots, I\}$, $G(\cdot)$ represents the standard Gaussian kernel, i_t denotes the *t*th pixel in the $\sqrt{T}\times\sqrt{T}$ region centered at the pixel *i*, $t \in \{1, 2, \ldots, T\}$. In (3) and (5), Gaussian kernel filtering is applied to reduce the effect of speckle noise on the distance measure [8]. Then, the final distance between the pixel feature representations $\mathbf{\Omega}(i)$ and $\mathbf{\Omega}(j)$ is calculated by combining the distances in (3)–(5)

$$D[\mathbf{\Omega}(i), \mathbf{\Omega}(j)] = \sqrt{\sum_{r=1}^{R}(\theta_r)^{\xi}[d_r(i,j)]^2} \tag{6}$$

where r = 1,2, …, R, $R = 5$ is the dimension of feature space, $0 < \theta_r < 1$ represents the weight of the *r*th feature, $\sum_{r=1}^{R}\theta_r = 1$, $\xi > 1$ is the amplification factor [27] of weights, and $i, j \in \{1, 2, \ldots, I\}$. Here, the amplification factor $\xi > 1$ aims at enhancing the features with large weights.

The distance measure in (6) may be affected by the dynamic ranges of different features. The normalization strategy for $\{d_r(i,j), r = 1, 2, \ldots, R\}$ in (6) will be discussed in Section IV-A.

IV. Proposed FVASS Algorithm

In this section, we introduce our new FVASS algorithm for superpixel segmentation of marine SAR images. It integrates the pixel feature representation strategy in (2) and the distance measure in (6). The key improvements of FVASS compared with other competing algorithms are the following ones: 1) FVASS incorporates not only the (commonly used) intensity and spatiality features, but also multiorder FV features to improve segmentation performance; and 2) FVASS adaptively controls the weights of the features according to the relative importance of such features in each iteration. A flowchart of the proposed FVASS algorithm is shown in Fig. 3.

FVASS is based on a linear iterative clustering strategy [26], and aims at producing superpixels with internally consistent features. We assume that there are *L* expected superpixels in the SAR image, where the centers of superpixels are indexed by $\{c_l, l = 1, 2, \ldots, L\}$. Based on the distance measure in (6), we define an energy function *E* [27] to measure the compactness of superpixels in the SAR image

$$E \triangleq \sum_{l=1}^{L}\sum_{i=1}^{I}\sum_{r=1}^{R}\upsilon_{i,l}(\theta_r)^{\xi}[d_r(i,c_l)]^2 \tag{7}$$

where $\upsilon_{i,l}$ denotes the pixel label, $\upsilon_{i,l} = 1$ if the *i*th pixel belongs to the *l*th superpixel and 0 otherwise, and $\sum_{l=1}^{L}\upsilon_{i,l} = 1$, $\forall i$. The energy function in (7) reflects the sum of within-superpixel variances of the SAR image. A smaller value of *E* in (7) is generally preferred since it is helpful to improve the internal consistency of the target and clutter superpixels in the SAR images. Therefore, superpixels are generated by minimizing the

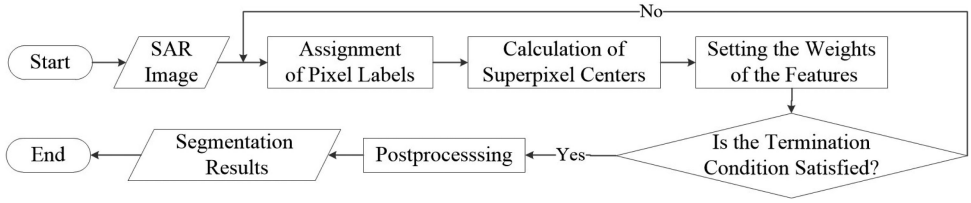

Fig. 3. Flowchart of the proposed FVASS algorithm.

energy function E

$$\left\{\hat{\upsilon}_{i,l},\ \hat{\mathbf{\Omega}}\left(c_l\right),\ \hat{\theta}_r,\quad \forall i,l,r\right\}=\min_{\left\{\upsilon_{i,l},\ \mathbf{\Omega}(c_l),\ \theta_r,\forall i,l,r\right\}} E$$
$$\text{s.t.}\ \sum_{r=1}^{R}\theta_r=1,\ \sum_{l=1}^{L}\upsilon_{i,l}=1\quad \forall i. \tag{8}$$

The optimization function in can be minimized by iteratively solving the following three subproblems (SBPs):

1) assigning the pixel labels;
2) updating the superpixel centers; and
3) adjusting the weights of features.

A. SBP-1: Pixel Label Assignment

First, we assign the pixel labels $\{\upsilon_{i,l},\forall i,l\}$ with the fixed superpixel centers and the weights of the features, i.e.,

$$\{\hat{\upsilon}_{i,l},\ \forall i,l\}=\min_{\{\upsilon_{i,l},\forall i,l\}} E,\quad \text{s.t.}\ \sum_{l=1}^{L}\upsilon_{i,l}=1\quad \forall i. \tag{9}$$

The solution of the optimization problem in (9) can be obtained by associating each pixel to its closest superpixel center in the SAR image. Since a superpixel represents a local coherent region, the search operation for each superpixel center is achieved in its neighboring $2S\times 2S$ region instead of the global image [9], where S is the expected size of the superpixel. Therefore, the solution of the optimization problem in (9) can be formulated as follows. For $\forall i\in\mathcal{N}_{2S\times 2S}(c_l)$, we have

$$\begin{cases}\hat{\upsilon}_{i,l}=1, & \text{if}\ \ D\left[\mathbf{\Omega}\left(i\right),\mathbf{\Omega}\left(c_l\right)\right]\\ & \le D\left[\mathbf{\Omega}\left(i\right),\mathbf{\Omega}\left(c_{l^*}\right)\right]\quad \forall\, l^*\in\Theta_i\\ \hat{\upsilon}_{i,l}=0, & \text{otherwise}\end{cases} \tag{10}$$

where $l=12,\ldots,L,\mathcal{N}_{2S\times 2S}(c_l)$ denotes the $2S\times 2S$ neighboring region centered at c_l. In (10), Θ_i denotes the index set of superpixel centers, where the distances from these centers to the ith pixel, $\{D[\mathbf{\Omega}(i),\mathbf{\Omega}(c_{l^*})],\ l^*\in\Theta_i\}$, have been calculated in advance. If $\Theta_i=\varnothing$, then $D[\mathbf{\Omega}(i),\mathbf{\Omega}(c_{l^*})]=+\infty$.

Having (6) in mind, we emphasize that the distance measure $D[\mathbf{\Omega}(i),\mathbf{\Omega}(c_l)]$ in (10) aggregates all the subdistances $\{d_r(i,c_l),r=1,2,\ldots,R\},\forall i,c_l$. The values of $\{d_r(i,c_l),\forall r\}$ should be normalized before (10) for fair comparison. Since the search area for each superpixel center is given by the $2S\times 2S$ neighboring pixels, each value in $\{d_r(i,c_l),\forall r\}$ for the lth superpixel center is prenormalized by using its corresponding maximum value in $\mathcal{N}_{2S\times 2S}(c_l)$.

B. SBP-2: Updating the Superpixel Centers

After the pixel labels have been assigned, the features of superpixel centers $\{\mathbf{\Omega}(c_l),\forall l\}$ are updated with the obtained (fixed) pixel labels and the weights of the features, i.e.,

$$\left\{\hat{\mathbf{\Omega}}\left(c_l\right),\quad \forall l\right\}=\min_{\{\mathbf{\Omega}(c_l),\forall l\}} E. \tag{11}$$

The solution of (11) is obtained by averaging the intensities, spatial coordinates, and the multiorder FV features of all the pixels corresponding to each superpixel

$$\hat{\mathbf{\Omega}}_r\left(c_l\right)=\frac{\sum_{i=1}^{I}\upsilon_{i,l}\mathbf{\Omega}_r\left(i\right)}{\sum_{i=1}^{I}\upsilon_{i,l}} \tag{12}$$

where $\mathbf{\Omega}_r(i)$ denotes the rth feature in $\mathbf{\Omega}(i)$, for $r=1,2,\ldots,R$, $l=1,2,\ldots,L$.

C. SBP-3: Adjusting the Weights of the Features

At this point, the weights of the features $\{\theta_r,\forall r\}$ are adjusted by minimizing the energy function E in (8) with the fixed pixel labels and superpixel centers

$$\left\{\hat{\theta}_r,\quad \forall r\right\}=\min_{\{\theta_r,\forall r\}} E,\quad \text{s.t.}\ \sum_{r=1}^{R}\theta_r=1. \tag{13}$$

The solution of (13) can be obtained by using the Lagrange multiplier method [22]

$$\hat{\theta}_r=\frac{1}{\sum_{r'=1}^{R}\left[sE_r/sE_{r'}\right]^{\frac{1}{\xi-1}}} \tag{14}$$

where $sE_r=\sum_{l=1}^{L}\sum_{i=1}^{I}\upsilon_{i,l}d_r^2(i,c_l)$denotes the within-superpixel variance of the rth feature in the SAR image, for $r=1,2,\ldots,R$. We refer readers to [27] for a detailed mathematical derivation of (14).

From (14), we can see that the features with smaller within-superpixel variances exhibit the larger weights values. In other words, we tend to emphasize the importance of the features with smaller within-superpixel variances, which are helpful to reduce the value of energy function E (i.e., enhancing the compactness of superpixels). Only a value of weight in $\{\hat{\theta}_r,\forall r\}$ is 1, while the other weights are 0, with $\xi\to 1^+$. In this case, the most important feature is the one used by FVASS. Each feature shares the same weight with $\xi\to+\infty$. In Section V-A, we evaluate the effect of the amplification factor ξ on the segmentation performance of FVASS.

Compared with the superpixel segmentation methods [7], [8], [10] involving the following two features: intensity and spatial

locations of pixels, FVASS may relatively weaken the effect of the spatiality feature, which is only one of five features to be considered. The spatiality feature is also important for superpixel generating because locally coherent superpixels are expected. To strength the effectiveness of the spatiality feature in superpixel generating, the within-superpixel variance $sE_{r=2}$ of the spatiality feature is replaced by

$$sE_{r=2} = \sum_{l=1}^{L}\sum_{i=1}^{I} \upsilon_{i,l} \Upsilon\left[d_{r=2}^2(i,c_l)\right] \tag{15}$$

where $\Upsilon[a] \triangleq \exp(-\zeta a)$ denotes a loss-pass filter and ζ is a constant. The loss-pass filter in (15) is helpful to remove $d_{r=2}^2(i,c_l)$ with large coefficient and further increase the weight of spatiality feature in (14). In this article, the constant ζ in (15) is adaptively set to 0.01*S*, which works well in the experiments. Note that the values of $\{sE_r, \forall r\}$ also need to be normalized before (14) to guarantee that they fall within the same dynamic range. Here, the normalization strategy for $\{sE_r, \forall r\}$ is

$$\begin{cases} sE_r = sE_r \Big/ \max\limits_{i,l}\left\{d_r^2(i,c_l)\right\}, & r = 1,3,4,5 \\ sE_r = sE_r \Big/ \max\limits_{i,l}\left\{\Upsilon\left[d_r^2(i,c_l)\right]\right\}, & r = 2. \end{cases} \tag{16}$$

The strategy for weight adjustment in FVASS differs from that in [13] and [14]. In (14), the weights of the features are controlled based on the relative performances of all features, instead of the performance of an individual feature (e.g., homogeneity degree), like in [13] and [14]. In this regard, it is our introspection that adjusting the weights using the relative importance of features may provide more robust superpixel segmentation results than only using the value of a specific feature. The strategy for weight setting in FVASS is also different from that in [19], [22], and [27], where the weight of the spatiality feature may be severely suppressed by other competitive features. This results in many tiny superpixels and increases the complexity of postprocessing. In the proposed FVASS algorithm, a low-pass filter in (15) is used to strengthen the effect of spatiality feature and generate local coherent regions.

Given the initial pixel labels, superpixel centers, and weights of features, the three SBPs in Section IV.A-C can be iteratively performed. The iterations are terminated when the number of iterations is larger than the predefined threshold *Iter*.

D. Postprocessing

Similar to other superpixel segmentation algorithms [7], [8], [10], [13], [14], the proposed FVASS algorithm does not explicitly enforce connectivity. When the iterative process of FVASS is terminated, a few disjoint superpixels may remain. To address this issue, disjoint superpixels should be merged into their neighboring superpixels to enhance connectivity. In this article, the postprocessing step in [9] is used to eliminate the disjointed pixels.

The detailed implementation of the proposed FVASS algorithm is given in Algorithm 1.

Algorithm 1: FVASS.

***Input*:** SAR image with *I* pixels, superpixel size *S*, amplification factor ξ, number of Gaussian components in GMM *M*, and maximum iteration count *Iter*.

Initialization: The expected number of superpixels in the image is $L = I/S^2$. Calculate FV for each pixel in the image by (1). Initialize the pixel labels $\upsilon_{i,l} = 0$, for $i = 1,2,\ldots,I, l = 1,2,\ldots,L$. Set the center of superpixels $\{c_l, \forall l\}$ with a regular grid interval *S*. The initialized weights are $\{\theta_r = 1/R, r = 1,2,\ldots,R\}$.

Iteration: **1)** Assign pixel labels. The temporary distances recorded by all the pixels are $\{\mathcal{D}_i = +\infty, \forall i\}$.

1.a) For the *l*-th superpixel center, c_l , calculate the distance $D[\mathbf{\Omega}(i), \mathbf{\Omega}(c_l)]$ between the *i*-th pixel and the center c_l via (6), for $\forall i \in \mathcal{N}_{2S\times 2S}(c_l)$.

1.b) If $D[\mathbf{\Omega}(i), \mathbf{\Omega}(c_l)] < \mathcal{D}_i$, then $\mathcal{D}_i = D[\mathbf{\Omega}(i), \mathbf{\Omega}(c_l)]$, $\hat{\upsilon}_{i,l} = 1$, else $\hat{\upsilon}_{i,l} = 0$, for $\forall i \in \mathcal{N}_{2S\times 2S}(c_l)$.

Repeat steps 1.a) and 1.b) for all the superpixel centers in the SAR image.

2) Update the intensities, spatial coordinates and multi-order FV features of superpixel centers $\{c_l, \forall l\}$ via (12).

3) Adjust the *r*-th weight θ_r via (14), for *r* = 1,2,…,*R*.

Until the number of iterations exceeds *Iter*.

Postprocessing: Merge disjoint superpixels into their neighbors via the postprocessing step as [9].

Output: Superpixels of the SAR image.

V. Experimental Results

In this section, we compare the superpixel segmentation performance and complexity of SLIC [10], pixel intensity and the location similarity (PILS) [8], exponential-SLIC (E-SLIC) [7], adaptive superpixel segmentation (ASS), and the proposed FVASS algorithm. The ASS algorithm is a degenerated version of FVASS, where the FV feature is not considered but the weights of the intensity and spatiality features are adaptively selected like in FVASS. Then, the five algorithms mentioned above are used for the superpixel generation module in existing superpixel-based ship detectors [4], [20] to evaluate the detection performance. Here, the results of superpixel segmentation algorithms based on image gradients [14] are not provided, since they are more suitable for SAR images in urban/land environments. *C*-band Gaofen-3 SAR images are used in this section to demonstrate the superiority of the proposed FVASS method. The key parameters of SAR images used in this section are shown in Table I. The ground truth of ship targets for Figs. 4–11 is provided in Fig. 4(b). The ground truth for Table II and Figs. 13–17 is obtained from [28], [31].

Without loss of generality, the size of the Gaussian kernel in (3) and (5) is 3×3. The amplification factor in FVASS is $\xi = 7$, and the number of Gaussian components in GMM is set to $M = 7$. The robustness of FVASS to the selection of hyperparameters, i.e., ξ and *M*, will be investigated in Figs. 9 and 10, respectively. The maximum number of iterations for FVASS is *Iter* = 10. The balancing parameters in SLIC, PILS, and E-SLIC are well tuned

TABLE I
KEY INFORMATION OF SAR IMAGES USED FOR EXPERIMENTS IN SECTION V

	Dataset for Figs. 4-12	Dataset for Table II and Figs. 13-17
Satellite	Gaofen-3	Gaofen-3
Polarization	HH	HH
Frequency Band	C	C
Centre Frequency	5.4 GHz	5.4 GHz
Angle of Incidence	20°-50°	20°-50°
Resolution	4m×4m	3m×3m
Size of Each Image Chip	254×228	256×256, 1000×1000
Number of Image Chips	101	1723, 1

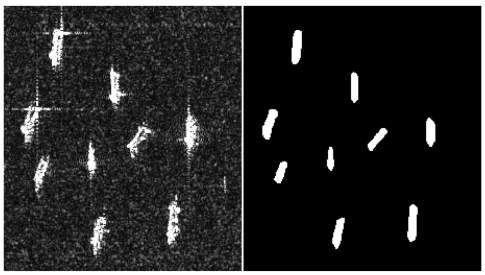

Fig. 4. (a) SAR image in a multitarget scenario. (b) Ground truth of ship targets.

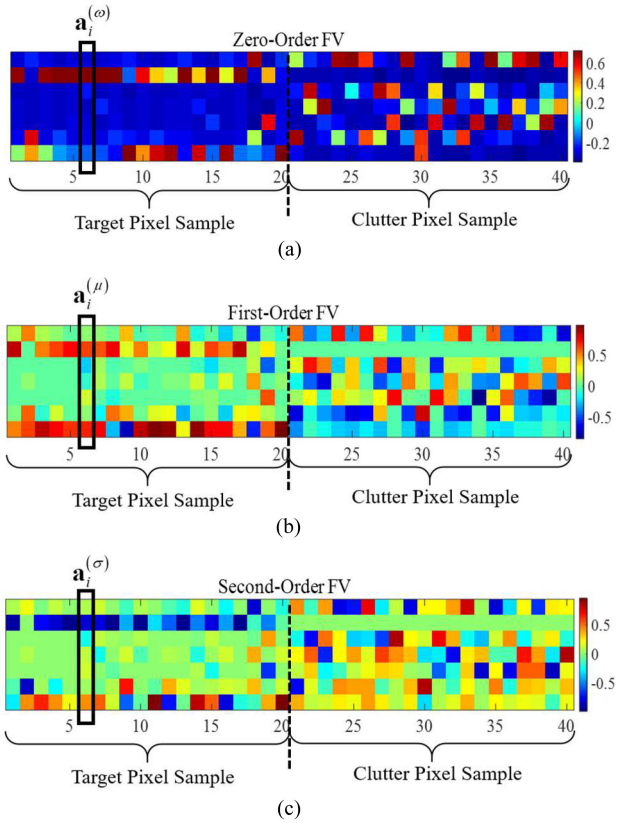

Fig. 5. Visualization of the (a) zero-order, (b) first-order, and (c) second-order FV features, where the number of Gaussian components in GMM is $M = 7$. Each column in (a)–(c) represents $\mathbf{a}_i^{(\omega)}$, $\mathbf{a}_i^{(\mu)}$, and $\mathbf{a}_i^{(\sigma)}$, respectively. There are 20 target pixel samples and 20 clutter pixel samples in each subfigure, which are randomly selected from Fig. 4(a).

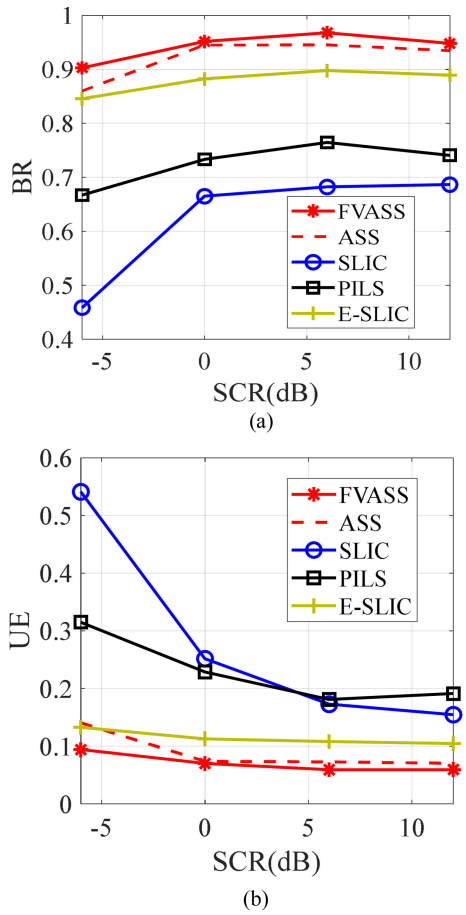

Fig. 6. BR and UE curves of the segmentation results in Fig. 4(a) with different SCR values, where $S = 24$. BR and UE values are averaged over 100 semicontrolled SAR images.

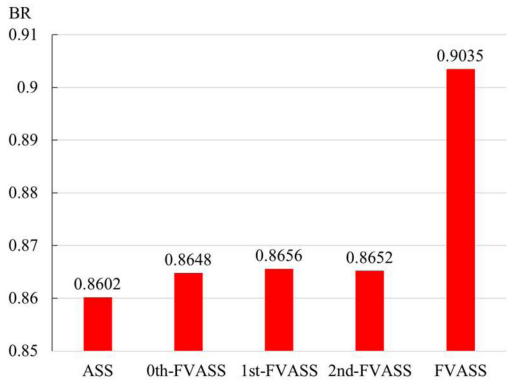

Fig. 7. BR values averaged over 100 semicontrolled SAR images, based on the reference image in Fig. 4(a) with SCR $= -6$dB and $S = 24$. The second to fourth columns represent that only the zero-order, first-order, or second-order FV feature is considered in FVASS, respectively. The fifth column denotes the full version of FVASS with the multiorder FV features.

in the high-SCR case (see Fig. 13), which are 0.1, 0.32, and 0.1 in the hereafter experiments, respectively.

The segmentation performance is quantitatively evaluated by two metrics, which are commonly used in the existing literature, i.e., boundary recall (BR) and undersegmentation error (UE) [9].

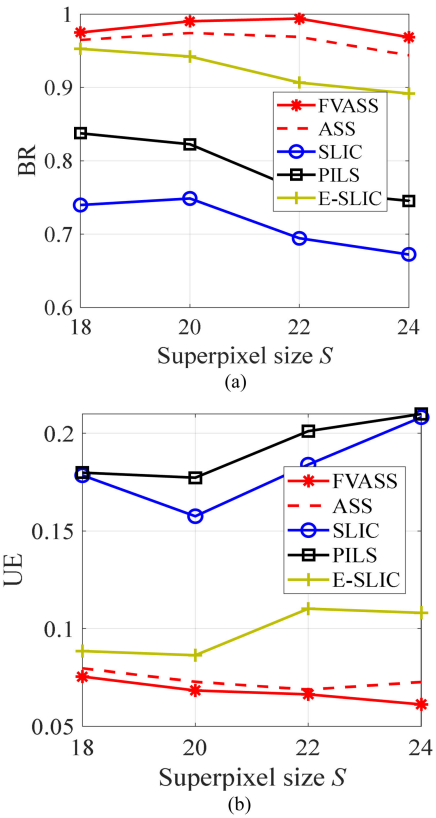

Fig. 8. BR and UE curves of the segmentation results in Fig. 4(a) with different values of the superpixel size S, where SCR = 3 dB. BR and UE values are averaged over 100 semicontrolled SAR images.

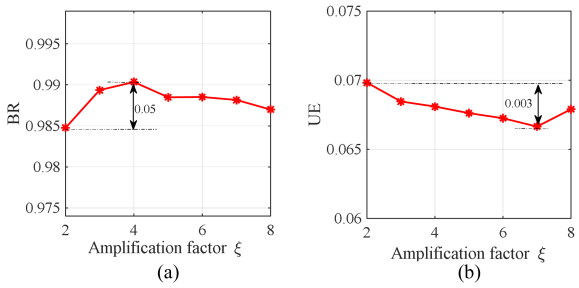

Fig. 9. Superpixel segmentation performance of the proposed FVASS algorithm versus the amplification factor ξ, where $M = 7$, $S = 20$, and SCR = 5 dB. (a) BR, (b) UE. BR and UE values are averaged over 100 semicontrolled SAR images, based on the reference image in Fig. 4(a).

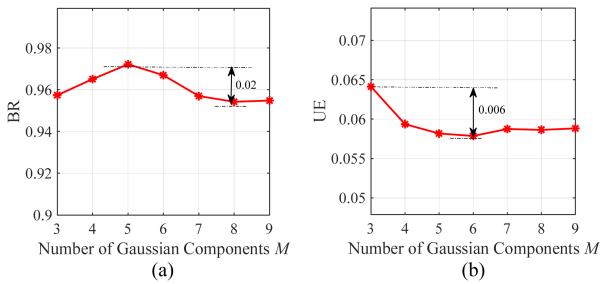

Fig. 10. Superpixel segmentation performance of the proposed FVASS algorithm versus the number of Gaussian components in GMM, where $\xi = 7$, $S = 24$, and SCR = 10 dB. (a) BR, (b) UE. BR and UE values are averaged over 100 semicontrolled SAR images, based on the reference image in Fig. 4(a).

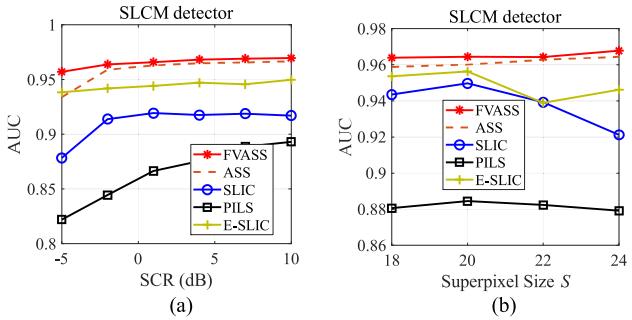

Fig. 11. Superpixel-based detection performance: AUC of SLCM [4] detector as a function of: (a) SCR, where $S = 24$, and (b) superpixel size S, where SCR = 3 dB. The AUC values are averaged over 100 semicontrolled SAR images, based on the reference image in Fig. 4(a).

TABLE II
AUC VALUES OF THE SLCM AND LCFV DETECTORS USING 1723 GAOFEN-3 IMAGES

	SLCM detector			LCFV detector		
	$S = 22$	$S = 24$	$S = 26$	$S = 22$	$S = 24$	$S = 26$
SLIC	0.8930	0.8883	0.8920	0.9095	0.9058	0.9077
PILS	0.9310	0.9253	0.9244	0.9501	0.9468	0.9525
E-SLIC	0.9748	0.9708	0.9748	0.9586	0.9554	0.9541
ASS	0.9662	0.9643	0.9662	0.9581	0.9554	0.9524
Proposed FVASS	**0.9793**	**0.9746**	**0.9792**	**0.9633**	**0.9668**	**0.9642**

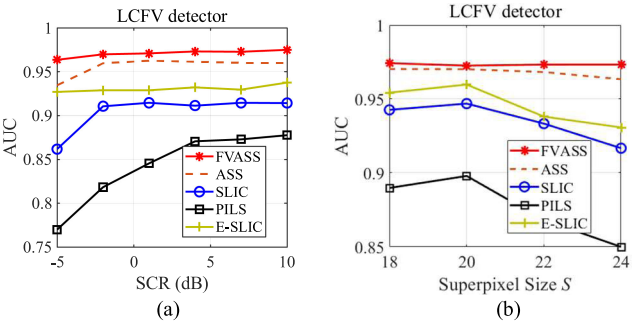

Fig. 12. Superpixel-based detection performance: AUC of LCFV [20] detector as a function of: (a) SCR, where $S = 24$, and (b) superpixel size S, where SCR = 3 dB. The AUC values are averaged over 100 semicontrolled SAR images, based on the reference image in Fig. 4(a).

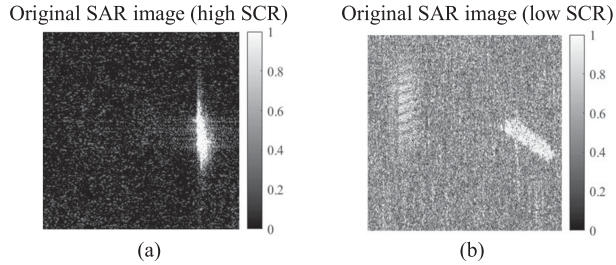

Fig. 13. Two SAR image samples [28] for visualization of superpixel segmentation and superpixel-based detection as shown in Figs. 14 and 15. (a) High SCR scenario. (b) Low SCR scenario.

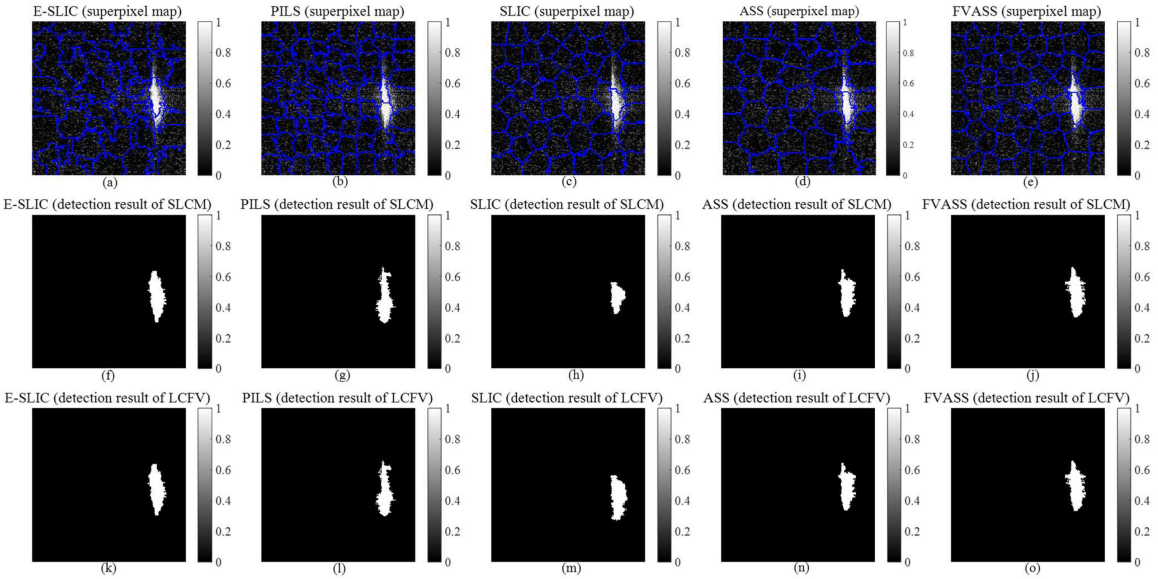

Fig. 14. Visualization of the superpixel segmentation and superpixel-based detection results of Fig. 13(a). (a)–(e) Superpixel segmentation results of E-SLIC, PILS, SLIC, ASS, and the proposed FVASS method, respectively, where $S = 26$. (f)–(o) Binary detection results of SLCM and LCFV detectors using the superpixels generated by the five above segmentation methods, respectively.

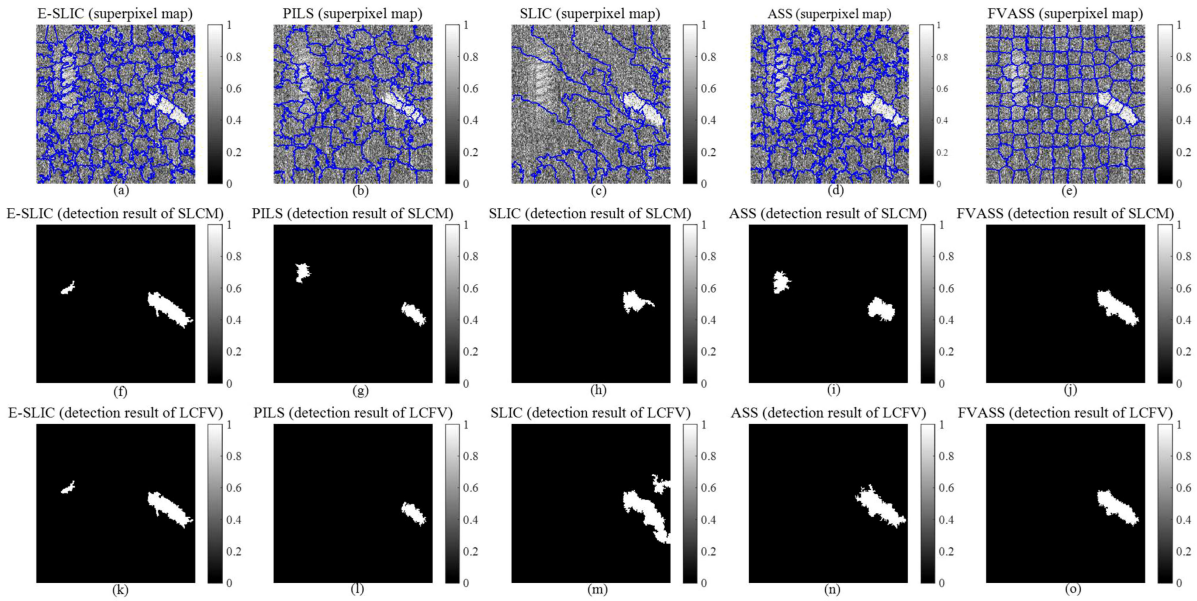

Fig. 15. Visualization of the superpixel segmentation and superpixel-based detection results of Fig. 13(b). (a)–(e) Superpixel segmentation results of E-SLIC, PILS, SLIC, ASS, and the proposed FVASS method, respectively, where $S = 22$. (f)–(o) Binary detection results of SLCM and LCFV detectors using the superpixels generated by the five above segmentation methods, respectively.

BR measures the boundary consistency between the produced superpixels and the ground truth of ship targets

$$\mathrm{BR} \triangleq \frac{1}{\left|\mathbf{B}^{(\mathbf{g})}\right|} \sum_{b \in \mathbf{B}^{(\mathbf{g})}} 1\left[\left(\min_{a \in \mathbf{B}^{(\mathbf{s})}} \sqrt{(x_a - x_b)^2 + (y_a - y_b)^2}\right) \leq \varepsilon\right] \tag{17}$$

where $\mathbf{B}^{(\mathbf{s})}$ and $\mathbf{B}^{(\mathbf{g})}$ are the sets of boundary pixels in the produced segmentation result and the ground truth, respectively, ε represents the bound parameter, $1[\cdot]$ is 1 if the input is true and 0 otherwise, and $|\cdot|$ represents the number of elements in a set. A larger value of BR indicates that the generated superpixels provide higher accuracy to maintain the boundaries of targets. In turn, UE evaluates the conciseness of the generated superpixels

$$\mathrm{UE} \triangleq \frac{\sum_{z=1}^{Z} \sum_{l=1}^{L} |\mathbf{s}_l| \times 1\left[|\mathbf{s}_l \cap \mathbf{g}_z| > \vartheta |\mathbf{s}_l|\right]}{\sum_{z=1}^{Z} |\mathbf{g}_z|} - 1 \tag{18}$$

where $\mathbf{s}_l$ and $\mathbf{g}_z$ denote the lth generated superpixel and zth ground truth segment in the SAR image, respectively, $l = 1, 2, \ldots, L$, $z = 1, 2, \ldots, Z$, and ϑ is the scale factor. A

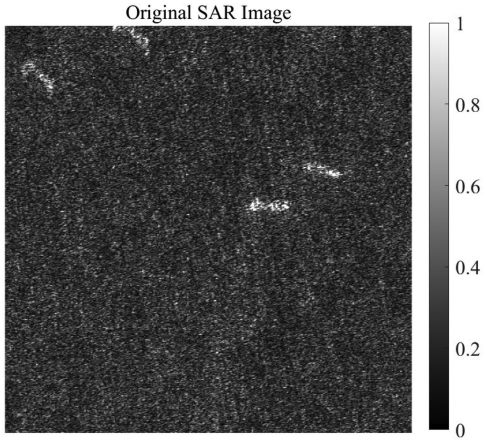

Fig. 16. Large SAR image [31] with four faint ship targets for the visualization of superpixel segmentation and superpixel-based detection as shown in Fig. 17.

smaller value of UE means that the produced superpixels have less overlapping between ship targets and the sea clutter. Note that the ground truth of SAR images may contain slight deviations or ambiguities, due to the motion and sidelobe of ship targets. This negligibly affects the quantitative evaluation of different methods because we set $\varepsilon = 3$ and $\vartheta = 0.01$ for (17) and (18), respectively, like in [9] and [22], instead of $\varepsilon = \vartheta = 0$.

We evaluate the performance of ship detection by using the area under the (receiver operating characteristic) curve (AUC) [29]. The probability of detection $P_{\rm d}$ and the probability of false alarm $P_{\rm fa}$ in AUC are defined by $P_{\rm d} = I_{\rm Dectar}/I_{\rm Tar}$, and $P_{\rm fa} = I_{\rm Falsala}/(I - I_{\rm Tar})$, respectively, where $I_{\rm Dectar}$, $I_{\rm Falsala}$, and $I_{\rm Tar}$ are the number of correctly detected target pixels, number of false alarm pixels, and number of target pixels in ground truth, respectively. Improvement of detection performance increases the value of AUC accordingly.

A. Experimental Results Based on Semicontrolled Data

In this section, we compare the superpixel segmentation performance and the further superpixel-based detection performance of different methods via semicontrolled data.

In Fig. 4, the SAR image in a multitarget scenario and the corresponding ground truth of ship targets are provided. Taking Fig. 4(a) as a reference image, semicontrolled SAR images are generated based on the guidelines in [29] to evaluate the performance of the proposed FVASS method in different SCR scenarios. Given the reference SAR image $\mathbf{U}$, the (pure) sea surface SAR image $\mathbf{V}$ and the value of SCR in dB, the semicontrolled SAR image is generated by

$$\bar{\mathbf{U}} = \mathbf{U} + \varsigma \mathbf{V} \tag{19}$$

where $\varsigma = \sqrt{10^{-{\rm SCR}/10} \sum_{i \in \mathbf{U}} \delta_i^2 / \sum_{j \in \mathbf{V}} \delta_j^2}$. From (19), it can be observed that the reference image is deteriorated with the decrease of SCR. In (19), the additive sea clutter [10], [29] is considered. We can also convert the multiplicative clutter/noise in SAR images to additive clutter/noise, as reported in [30]. We refer readers to [29, Fig. 8] for semicontrolled SAR images with different SCRs.

In Fig. 5, we visualize the vectors of $\mathbf{a}_i^{(\omega)}$, $\mathbf{a}_i^{(\mu)}$, and $\mathbf{a}_i^{(\sigma)}$ in (1) to show the effectiveness of the multiorder FV features used in the proposed FVASS method. It is observed that target and clutter pixels show dissimilarity in terms of zero-order, first-order, and second-order features in FVs. This benefits the superpixel generation task because the blend between target and clutter pixels within a superpixel can be reduced based on FVs.

Fig. 6 depicts the BR and UE curves of SLIC, PILS, E-SLIC, ASS, and the proposed FVASS algorithm with different SCR values, where BR and UE values are obtained by averaging over 100 semicontrolled SAR images. In Fig. 6, PILS, E-SLIC, and ASS perform better than SLIC in low-SCR case since they contain smoothing filters to suppress the speckle noise in SAR images, while SLIC does not. The proposed FVASS method provides larger BR and smaller UE values than other methods. This is because the newly added multiorder FV features in FVASS improve the discrimination between ship targets and the sea clutter, and the weights of the features considered in FVASS are adaptively adjusted to enhance its robustness to different SCRs. It is worth mentioning that FVASS provides a better segmentation performance than ASS especially in low-SCR cases. This demonstrates the robustness of FV to the strong sea clutter background in SAR images. In Fig. 7, we further show the effectiveness of the multiorder features in FVs, where the BR value produced by ASS is used as a reference due to its good performance in Fig. 6(a). From Fig. 7, we can see that FVASS provides a better segmentation performance even with only one of the multiorder FV features in low-SCR cases. This confirms the superiority of FVs for the superpixel segmentation in marine SAR images again.

The value of S is a key input parameter determining the expected size of superpixels. The authors in [4], [10], and [20] suggest that the superpixel size S can be selected based on a predefined percentage (e.g., 25%) of the number of pixels in the area occupied by a ship target. Due to the diversity of the size of ship targets, we also evaluate the segmentation performance of different methods versus the value of superpixel size S. As depicted in Fig. 8, the proposed FVASS algorithm provides larger BR and smaller UE values than other methods, with different values of the superpixel size. Besides, FVASS is less sensitive to the superpixel size S than SLIC, E-SLIC, and PILS.

Fig. 9 shows the effect of the amplification factor ξ in (14) on the performance of the proposed FVASS method. BR and UE values are averaged over 100 semicontrolled SAR images, where the reference image is Fig. 4(a). It can be observed that the perturbations of BR and UE values are only 0.005 and 0.003, respectively, in the case of $\xi \in \{2, 3, \ldots, 8\}$. In Fig. 10, we investigate the performance of FVASS versus the hyperparameter M, i.e., the number of Gaussian components in GMM. FVASS provides similar BR and UE values with $M \in \{3, 4, \ldots, 9\}$, where the perturbations of BR and UE values are only 0.02 and 0.006, respectively.

In Figs. 11 and 12, we show the detection performance of two recently proposed superpixel-based ship detectors, i.e., superpixel-based local contrast measure (SLCM) [4] and local contrast of FV (LCFV) [20], respectively. The SLCM detector is developed based on the difference of intensities between

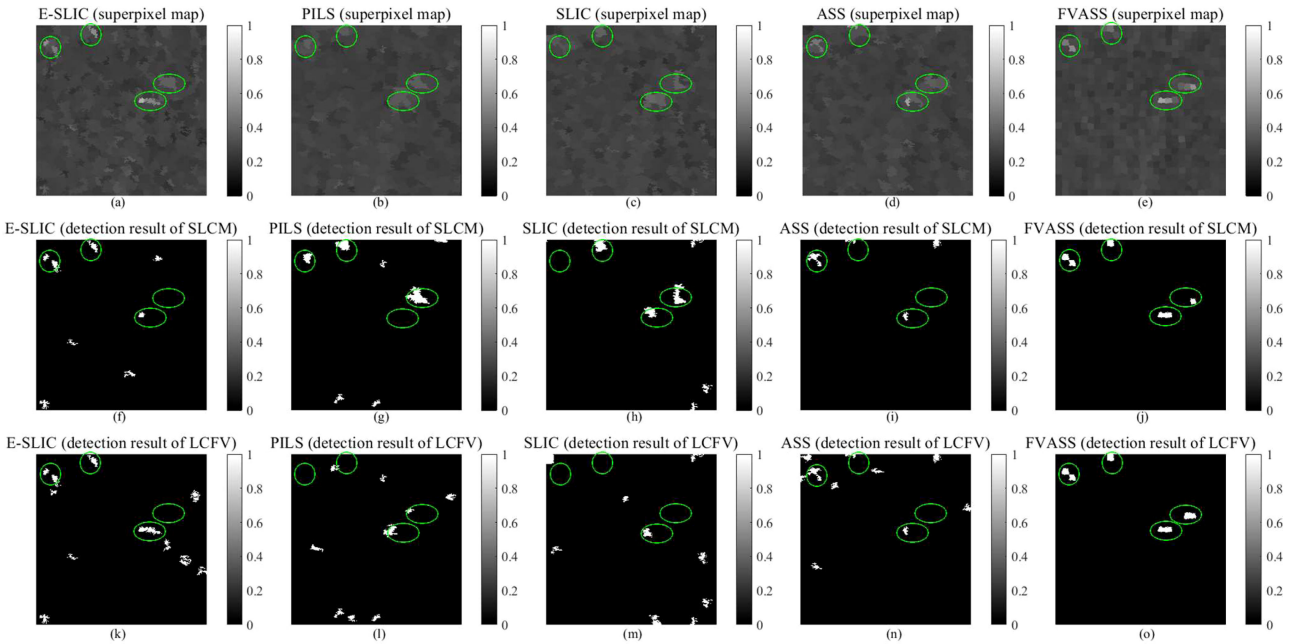

Fig. 17. Visualization of the superpixel segmentation and superpixel-based detection results of Fig. 16. (a)–(e) Superpixel segmentation results of E-SLIC, PILS, SLIC, ASS, and the proposed FVASS method, respectively, where $S = 38$. (f)–(o) Binary detection results of SLCM and LCFV detectors using the superpixels generated by the five above segmentation methods, respectively. The ground truth of targets is represented using green ellipses.

the target and its surrounding clutter superpixels. The LCFV detector exploits the contextual dissimilarity of superpixel-based FVs. The detection frameworks of SLCM and LCFV both require the superpixel segmentation step as the preprocessing of SAR images. We refer readers to [4] and [20] for the implementations of SLCM and LCFV, respectively. Here, five superpixel segmentation algorithms, i.e., SLIC, PILS, E-SLIC, ASS, and FVASS are used for the superpixel segmentation step in the aforementioned two detectors. As shown in Figs. 11 and 12, the proposed FVASS algorithm results in improved detection performance, thanks to its better superpixel segmentation performance, as reported in Figs. 6 and 8. Note that FVASS achieves a better detection performance than ASS especially in low-SCR cases (e.g., SCR $= -5$dB), which is consistent with results in Fig. 6. This demonstrates the superiority of FVASS again.

B. Experimental Results Based on Real Data

In this section, we compare SLIC, PILS, E-SLIC, ASS, and the proposed FVASS algorithm by using Gaofen-3 images [28], [31] in terms of the superpixel-based detection performance and the running time. The aforementioned five segmentation algorithms are employed in the superpixel generating step of SLCM [4] and LCFV [20] detectors, respectively. The ground truth of ship targets for SAR images is provided as rectangle regions (see [28, Fig. 7]), which may contain a few clutter pixels. Therefore, the following steps are used to remove the potential clutter pixels in rectangle target regions labeled by [28]: 1) The Ostu method is applied to segment the rectangle target regions and obtain the binary results, where the areas of "1" (coarsely) represent the target pixels. 2) Isolated clutter pixels are eliminated via the opening operation. The target areas generated by using the abovementioned two steps are considered as the ground truth of ship targets.

In Table II, we show the AUC values obtained for the SLCM and LCFV detectors, respectively, based on 1723 Gaofen-3 SAR images. We can observe from Table II that the proposed FVASS superpixel segmentation method leads to a better ship detection performance as compared with other competing methods. In Fig. 13, we provide two SAR image samples from the dataset in Table I to visually show the superiority of the proposed FVASS method. Fig. 14 illustrates the superpixel segmentation maps and superpixel-based detection results corresponding to SLIC, E-SLIC, PILS, ASS, and FVASS in the scenario with the high SCR. From Fig. 14(a)–(e), we can see that the outline of the ship target is well marked by all the superpixel segmentation methods in the high-SCR case. Besides, the ship target is correctly detected by using superpixel-based SLCM [4] and LCFV [20] detectors, as shown in Fig. 14(f)–(o). Fig. 15 shows the segmentation and detection results in the low SCR scenario. From Fig. 15(a)–(e), we can observe that FVASS approximately maintains the boundary of the weak ship target and generates compact clutter superpixels. However, PILS, SLIC, E-SLIC, and ASS provide irregular boundaries of superpixels. Fig. 15(f)–(o) shows that the ship detectors based on the superpixels generated by FVASS provide a better detection performance, i.e., fewer false alarms and more correctly detected target areas. This demonstrates the superiority of FVASS in low-SCR cases, thanks to the newly considered FV feature and the adaptive weights of the features.

Fig. 16 shows an SAR image with 1000×1000 pixels, in which four faint ship targets are contained. In Fig. 17, we illustrate the superpixel segmentation results and the corresponding detection results based on Fig. 16. For SLIC, PILS, and E-SLIC, we continue to use the balancing parameters well-tuned in

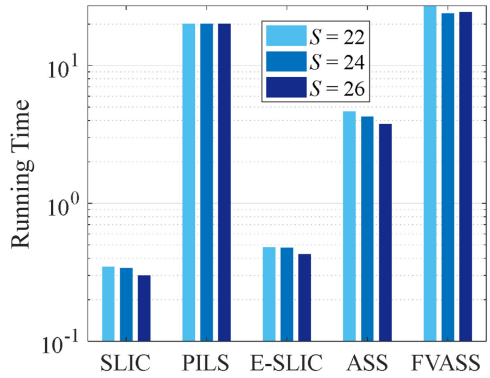

Fig. 18. Comparison of the running time (seconds) with different values of the superpixel size S. Each value of the running time is averaged over 1723 SAR images. Each SAR image contains 256×256 pixels.

Fig. 13 with a high SCR. Note that the sizes of superpixels are much smaller than that of the large SAR image. Accordingly, each pixel in the superpixel maps of Fig. 17(a)–(e) is replaced by the average intensity of its corresponding superpixel to effectively visualize the segmentation results. From Fig. 17(a)–(e), it can be observed that the proposed FVASS method highlights better the weak ship targets than other existing methods. As shown in Fig. 17(f)–(o), E-SLIC, PILS, SLIC, and ASS lead to some missed targets and false alarms, while FVASS still accurately locates ship targets.

In Fig. 18, we compare the running times of SLIC, PILS, E-SLIC, ASS, and the proposed FVASS method, where each value is calculated by averaging over 1723 Gaofen-3 SAR images. Experiments are performed in a desktop with a 64-b Windows operating system, a 128-GB of RAM, and an Intel Xeon CPU. The software platform is MATLAB (2019a). From Fig. 18, it can be seen that SLIC is the fastest algorithm due to its simplicity. Compared with the other methods, FVASS requires the calculation of FVs, which results in an affordable increase of computational burden. The FVs calculated for superpixel segmentation can also be used for the subsequent superpixel-based target detection [10], [20] saving computational time.

VI. Conclusion

In this article, a new algorithm called FVASS was developed for superpixel segmentation of SAR images. In addition to the commonly used intensity and spatiality features, the multiorder characteristics contained in FVs are incorporated in FVASS (for the first time in the literature) to enhance the performance of pixel representation in SAR images. Besides, FVASS iteratively adjusts the weights of the features by minimizing the global within-superpixel variance of features, to guarantee the compactness of superpixels. Experimental results verify the effectiveness of the proposed FVASS method compared with existing approaches especially in low-SCR cases (in terms of not only superpixel segmentation performance, but also the subsequent superpixel-based ship detection performance) with an affordable increase of computational complexity. The extension of our newly developed FVASS to more complex backgrounds, e.g., ship targets in inshore and surrounding-the-island scenarios, will be pursued in future research.

Acknowledgment

The authors would like to thank the Associate Editor and anonymous reviewers for their helpful suggestions, which improved the quality of this article.

References

[1] Y. Zhao, L. Zhao, B. Xiong, and G. Kuang, "Attention receptive pyramid network for ship detection in SAR images," *IEEE J. Sel. Topics Appl. Earth Observ. Remote Sens.*, vol. 13, pp. 2738–2756, 2020.

[2] X. Wang, G. Li, A. Plaza, and Y. He, "Ship detection in SAR images via enhanced nonnegative sparse locality-representation of Fisher vectors," *IEEE Trans. Geosci. Remote Sens.*, to be published, doi: 10.1109/TGRS.2020.3042506.

[3] T. Li, Z. Liu, R. Xie, and L. Ran, "An improved superpixel-level CFAR detection method for ship targets in high-resolution SAR images," *IEEE J. Sel. Topics Appl. Earth Observ. Remote Sens.*, vol. 11, no. 1, pp. 184–194, Jan. 2018.

[4] X. Wang, C. Chen, Z. Pan, and Z. Pan, "Superpixel-based LCM detector for faint ships hidden in strong noise background SAR imagery," *IEEE Geosci. Remote Sens. Lett.*, vol. 16, no. 3, pp. 417–421, Mar. 2019.

[5] O. Pappas, A. Achim, and D. Bull, "Superpixel-level CFAR detectors for ship detection in SAR imagery," *IEEE Geosci. Remote Sens. Lett.*, vol. 15, no. 9, pp. 1397–1401, Sep. 2018.

[6] J. Guo, X. Zhou, J. Li, A. Plaza, and S. Prasad, "Superpixel-based active learning and online feature importance learning for hyperspectral image analysis," *IEEE J. Sel. Topics Appl. Earth Observ. Remote Sens.*, vol. 10, no. 1, pp. 347–359, Jan. 2017.

[7] W. Yu, Y. Wang, H. Liu, and J. He, "Superpixel-based CFAR target detection for high-resolution SAR images," *IEEE Geosci. Remote Sens. Lett.*, vol. 13, no. 5, pp. 730–734, May 2016.

[8] D. Xiang, T. Tang, L. Zhao, and Y. Su, "Superpixel generating algorithm based on pixel intensity and location similarity for SAR image classification," *IEEE Geosci. Remote Sens. Lett.*, vol. 10, no. 6, pp. 1414–1418, Nov. 2013.

[9] R. Achanta, A. Shaji, K. Smith, A. Lucchi, P. Fua, and S. Süsstrunk, "SLIC superpixels compared to state-of-the-art superpixel methods," *IEEE Trans. Pattern Anal. Mach. Intell.*, vol. 34, no. 11, pp. 2274–2282, Nov. 2012.

[10] H. Lin, H. Chen, K. Jin, L. Zeng, and J. Yang, "Ship detection with superpixel-level Fisher vector in high-resolution SAR images," *IEEE Geosci. Remote Sens. Lett.*, vol. 17, no. 2, pp. 247–251, Feb. 2020.

[11] E. Akyilmaz and U. M. Leloglu, "Similarity ratio based adaptive mahalanobis distance algorithm to generate SAR superpixels," *Can. J. Remote Sens.*, vol. 43, no. 6, pp. 569–581, 2017.

[12] J. Feng, Z. Cao, and Y. Pi, "Polarimetric contextual classification of PolSAR images using sparse representation and superpixels," *Remote Sens.*, vol. 6, no. 8, pp. 7158–7181, Jul. 2014.

[13] D. Xiang, Y. Ban, W. Wang, and Y. Su, "Adaptive superpixel generation for polarimetric SAR images with local iterative clustering and SIRV model," *IEEE Trans. Geosci. Remote Sens.*, vol. 55, no. 6, pp. 3115–3131, Jun. 2017.

[14] D. Xiang, T. Tang, S. Quan, D. Guan, and Y. Su, "Adaptive superpixel generation for SAR images with linear feature clustering and edge constraint," *IEEE Trans. Geosci. Remote Sens.*, vol. 57, no. 6, pp. 3873–3889, Jun. 2019.

[15] D. Xiang *et al.*, "Adaptive statistical superpixel merging with edge penalty for PolSAR image segmentation," *IEEE Trans. Geosci. Remote Sens.*, vol. 58, no. 4, pp. 2412–2429, Apr. 2020.

[16] W. Jing, T. Jin, and D. Xiang, "Edge-Aware superpixel generation for SAR imagery with one iteration merging," *IEEE Geosci. Remote Sens. Lett.*, to be published, doi: 10.1109/LGRS.2020.3005973.

[17] R. Shang, J. Lin, L. Jiao, X. Yang, and Y. Li, "Superpixel boundary-based edge description algorithm for SAR image segmentation," *IEEE J. Sel. Topics Appl. Earth Observ. Remote Sens.*, vol. 13, pp. 1971–1985, 2020.

[18] W. Wang, D. Xiang, Y. Ban, J. Zhang, and J. Wan, "Superpixel segmentation of polarimetric SAR images based on integrated distance measure and entropy rate method," *IEEE J. Sel. Topics Appl. Earth Observ. Remote Sens.*, vol. 10, no. 9, pp. 4045–4058, Sep. 2017.

[19] X. Wang, G. Li, and A. Plaza, "Adaptive superpixel segmentation with Fisher vectors for ship detection in SAR images," presented at the IEEE Int. Geosci. Remote Sens. Symp., 2020.
[20] X. Wang, G. Li, X. Zhang, and Y. He, "Ship detection in SAR images via local contrast of Fisher vectors," *IEEE Trans. Geosci. Remote Sens.*, vol. 58, no. 9, pp. 6467–6479, Sep. 2020.
[21] T. Ahonen, A. Hadid, and M. Pietikainen, "Face description with local binary patterns: Application to face recognition," *IEEE Trans. Pattern Anal. Mach. Intell.*, vol. 28, no. 12, pp. 2037–2041, Dec. 2006.
[22] X. Xiao, Y. Zhou, and Y. Gong, "Content-Adaptive superpixel segmentation," *IEEE Trans. Image Process.*, vol. 27, no. 6, pp. 2883–2896, Jun. 2018.
[23] J. Sánchez, F. Perronnin, T. Mensink, and J. Verbeek, "Image classification with the Fisher vector: Theory and practice," *Int. J. Comput. Vis.*, vol. 105, no. 3, pp. 222–245, 2013.
[24] Q. Chen *et al.*, "Efficient maximum appearance search for large-scale object detection," in *Proc. IEEE Conf. Comput. Vis. Pattern Recognit.*, Portland, OR, USA, 2013, pp. 3190–3197.
[25] T. Celik and T. Tjahjadi, "Automatic image equalization and contrast enhancement using Gaussian mixture modeling," *IEEE Trans. Image Process.*, vol. 21, no. 1, pp. 145–156, Jan. 2012.
[26] T. K. Moon, "The expectation-maximization algorithm," *IEEE Signal Process. Mag.*, vol. 13, no. 6, pp. 47–60, Nov. 1996.
[27] J. Z. Huang, M. K. Ng, H. Rong, and Z. Li, "Automated variable weighting in k-means type clustering," *IEEE Trans. Pattern Anal. Mach. Intell.*, vol. 27, no. 5, pp. 657–668, May 2005.
[28] Y. Wang, C. Wang, H. Zhang, Y. Dong, and S. Wei, "A SAR dataset of ship detection for deep learning under complex backgrounds," *Remote Sens.*, vol. 11, no. 7, pp. 765, 2019.
[29] G. Xiong, F. Wang, L. Zhu, J. Li, and W. Yu, "SAR target detection in complex scene based on 2-D singularity power spectrum analysis," *IEEE Trans. Geosci. Remote Sens.*, vol. 57, no. 12, pp. 9993–10003, Dec. 2019.
[30] S. Liu, M. Liu, P. Li, J. Zhao, Z. Zhu, and X. Wang, "SAR image denoising via sparse representation in shearlet domain based on continuous cycle spinning," *IEEE Trans. Geosci. Remote Sens.*, vol. 55, no. 5, pp. 2985–2992, May 2017.
[31] X. Sun, Z. Wang, Y. Sun, W. Diao, Y. Zhang, and K. Fu, AIR-SARShip-1.0: High-resolution SAR ship detection dataset, *J. Radars*, vol. 8, no.no. 6, pp. 852–862, 2019.

Xueqian Wang (Member, IEEE) received the B.S. and Ph.D. degrees in electronic engineering from the University of Electronic Science and Technology of China, Chengdu, China, in 2015, and Tsinghua University, Beijing, China, in 2020, respectively.

He is currently a Postdoctoral Fellow with the Department of Electronic Engineering, Tsinghua University. From 2018 to 2019, he visited Syracuse University, Syracuse, NY, USA. His main research interests include target detection, information fusion, radar imaging, compressed sensing, and distributed signal processing.

You He received the Ph.D. degree in electronic engineering from Tsinghua University, Beijing, China, in 1997.

He is currently a Professor with Naval Aeronautical University, Yanta, China. He is also cross-appointed to the Department of Electronic Engineering, Tsinghua University. He has authored or coauthored 300 academic articles. He is the author of *Radar Target Detection and CFAR Processing* (Tsinghua University Press) and *Multi-Sensor Information Fusion With Applications and Radar Data Processing With Applications* (Publishing House of Electronics Industry). His current research interests include detection and estimation theory, CFAR processing, distributed detection theory, and multisensor information fusion.

Dr. He is also a Fellow Member of the Chinese Academy of Engineering. In 2017, he was a recipient of the Top Prize in Science and Technology of Shandong Province. He currently serves on the editorial boards for the *Journal of Data Acquisition and Processing*, *Modern Radar*, *Fire Control and Command Control*, and *Radar Science and Technology*.

Gang Li (Senior Member, IEEE) received the B.S. and Ph.D. degrees in electronic engineering from Tsinghua University, Beijing, China, in 2002 and 2007, respectively.

Since July 2007, he has been with the Faculty of Tsinghua University, where he is currently a Professor with the Department of Electronic Engineering. From 2012 to 2014, he visited Ohio State University, Columbus, OH, USA, and Syracuse University, Syracuse, NY, USA. He has authored or coauthored more than 160 journal and conference papers. He is the author of Advanced Sparsity-Driven Models and Methods for Radar Applications. His research interests include radar imaging, distributed signal processing, sparse signal processing, micro-Doppler analysis, and information fusion.

Dr. Li is currently an Associate Editor for the IEEE TRANSACTIONS ON SIGNAL PROCESSING.

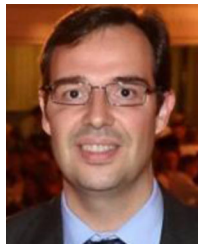

Antonio Plaza (Fellow, IEEE) received the M.Sc. and Ph.D. degrees in computer engineering from Hyperspectral Computing Laboratory, Department of Technology of Computers and Communications, University of Extremadura, Cáceres, Spain, in 1999 and 2002, respectively.

He is the Head of the Hyperspectral Computing Laboratory, Department of Technology of Computers and Communications, University of Extremadura. He has authored more than 600 publications, including more than 200 JCR journal articles (more than 160 in IEEE journals), 23 book chapters, and around 300 peer-reviewed conference proceeding papers. His research interests include hyperspectral data processing and parallel computing of remote sensing data.

Dr. Plaza was a member of the editorial board of the IEEE GEOSCIENCE AND REMOTE SENSING NEWSLETTER from 2011 to 2012 and the *IEEE Geoscience and Remote Sensing Magazine*, in 2013. He was also a member of the Steering Committee of the IEEE JOURNAL OF SELECTED TOPICS IN APPLIED EARTH OBSERVATIONS AND REMOTE SENSING (JSTARS). He is also a fellow of IEEE for contributions to hyperspectral data processing and parallel computing of earth observation data. He was the recipient of the recognition as the Best Reviewer of the IEEE GEOSCIENCE AND REMOTE SENSING LETTERS, in 2009 and the IEEE TRANSACTIONS ON GEOSCIENCE AND REMOTE SENSING, in 2010, for which he was an Associate Editor from 2007 to 2012, and the Most Highly Cited Paper (2005–2010) in the *Journal of Parallel and Distributed Computing*, the 2013 Best Paper Award of the IEEE JSTARS, the Best Column Award of the *IEEE Signal Processing Magazine*, in 2015, and at the IEEE International Conference on Space Technology and the IEEE Symposium on Signal Processing and Information Technology. He was the Director of Education Activities for the IEEE Geoscience and Remote Sensing Society (GRSS) from 2011 to 2012 and the President of the Spanish Chapter of the IEEE GRSS from 2012 to 2016. He has reviewed more than 500 manuscripts for over 50 different journals. He was the Editor-in-Chief for the IEEE TRANSACTIONS ON GEOSCIENCE AND REMOTE SENSING from 2013 to 2017. He has guest-edited ten special issues on hyperspectral remote sensing for different journals. He is also an Associate Editor for the IEEE ACCESS (received the recognition as an Outstanding Associate Editor of the journal in 2017). For more information please visit http://www.umbc.edu/rssipl/people/aplaza